Additive Manufacturing 101 (2025) 104714

Contents lists available at ScienceDirect

Additive Manufacturing

journal homepage: www.elsevier.com/locate/addma

Smooth 3D transition cell generation based on latent space arithmetic

Xiaochen Yu [1], Bohan Peng [1], Ajit Panesar [*]

IDEA Lab, Department of Aeronautics, Imperial College London, SW7 2AZ, UK

ARTICLE INFO

Keywords:
Latent space
Data-driven design
Lattices

ABSTRACT

Lattice structures with multiple unit cell types diversify the property space by offering more design freedom, encouraging adaptation of metamaterials in engineering applications. It is essential to ensure structural connectivity and smooth transition among different cell types to avoid pre-mature failure. In this work, we propose a framework based on latent space operations to generate smoothly morphing and fully connected transition cells, addressing the current research gap in realising lattice designs of dissimilar unit cells. Latent embedding – a low-dimensional representation of the original microstructure – is obtained through a variational autoencoder. Different types of triply periodic minimal surface (TPMS) lattice were chosen as the targets to demonstrate the capability of the algorithm in handling complex 3D geometries within a physically restricted transition region. Both qualitative and quantitative evaluations are provided to illustrate the connectivity and geometric similarity of the generated transition. Benchmark comparisons against both analytical and existing machine learning (ML) based solutions indicate the superior efficacy and generality of the proposed framework.

1. Introduction

Advancements in additive manufacturing (AM) have enabled the fabrication of lattice structures with complex geometric features. Composed of one or more types of repeating unit cells [1], lattice is widely adopted in structural applications due to its high strength-to-weight ratio [2,3], energy absorption capability [4–7], and robustness to load variability [8]. Beyond mechanical advantages, lattice structures also excel in other functional aspects such as heat dissipation [9–11] and vibration isolation [12–14]. Depending on whether there is spatial variation in the unit cell's volume fraction, lattice structures can be categorized as uniform or graded [15]. The latter enables functionally graded design from the macro-scale level. However, both uniform and graded cases are typically restricted to a single unit cell topology, greatly limiting design flexibility.

Studies have demonstrated that the property space could be further diversified by adopting a multi-unit-cell configuration [16,17], that is, introducing different unit cell types within a single macro-structure. Ensuring connectivity and smooth transition among diverse unit cells becomes an emerging consideration to be addressed. Otherwise, abrupt changes and insufficient connection will likely result in stress concentration and pre-mature failure [18]. In response, Wang et al. [19] reformulated the microstructure assembly problem as a label selection task on a weighted graph, aiming to minimise both nodal weights (i.e. property deviation of the selected microstructure from the target) and edge weights (i.e. geometric and mechanical incompatibility between pairs). The same research group also investigated one-to-many property-to-design mapping at the microstructure level by conducting k-means clustering within the Laplace-Beltrami spectrum, which increases the probability of boundary compatibility during assembly [20]. Despite the efforts, a common compromise is to adhere to cell types with inherently matching boundaries. There is a lack of generative design strategies that directly tackle the connectivity challenge.

Latent space arithmetic has gained popularity in the field of image processing, which inspired the data-driven design of metamaterials. The latent vector is a reduced-dimension representation of the original input data where only essential features were preserved. It could be obtained by training a generative ML model called autoencoder. The input is first transformed into the latent space through an encoder via convolution operations, followed by a reverse process to decode the latent vector back to a high-dimension feature space. Smooth image-to-image translation was achieved by interpolating within the latent space. For instance, Chen et al. [21] introduced a control vector into the linear interpolation formula, enabling the alternation of target attributes by selecting a specific interpolation path. Mi et al. [22] investigated the domain dependency of different interpolation methods. Liu et al. [23]

* Corresponding author.
E-mail address: a.panesar@imperial.ac.uk (A. Panesar).

[1] These authors contributed equally.

https://doi.org/10.1016/j.addma.2025.104714
Received 9 August 2024; Received in revised form 13 January 2025; Accepted 17 February 2025
Available online 18 February 2025
2214-8604/

proposed regularisation techniques to improve the performance of inter-domain interpolation, alleviating the issue of non-realistic intermediate images. The volumetric representation of a structure shares a similar data format as an image, where an array is used to indicate material existence at each voxel. Consequently, geometry manipulation was also explored by applying arithmetic among latent vectors [24,25]. For example, in the semantic operation of ‘cube with hole’ - ‘cube’ + ‘sphere’ = ‘sphere with hole’, each geometry is represented by a latent vector, and the result of the arithmetic operation on these vectors directly maps to the resulting geometry.

The work conducted by Baldwin et al. [26] applied latent space interpolation to generate multi-unit-cell transitions for 2D parameterised geometries. The impact on smoothness level was investigated by varying the distance between two endpoints in latent space and the number of interpolation points. A follow-up work [27] explored whether integrating property into the latent embedding is advantageous over the sole consideration of geometric features. However, the smoothness metric proposed here is a measurement of geometric similarity between unit cells instead of connectivity. Although a series of unit cells that were visually smooth in transition was generated through latent space interpolation, it remained an open question on how a transition cell bounded by a finite design domain could be generated while preserving the smooth characteristics from latent space operation.

This paper aims to address the current research gap of generating smoothly morphing, fully connected transition cell between dissimilar unit cells within a confined space to realise multi-unit-cell lattice designs. It is achieved through the proposed framework utilising both latent space arithmetic and feature space operations, whilst expanding the design space to include 3D complex geometries. The steps involved in retrieving latent representation by training a variational autoencoder (VAE) model, and operations required to construct the transition cell are first elaborated in detail. The performance of the proposed framework is evaluated both qualitatively and quantitatively (i.e. via interfacial connectivity and geometric similarity metrics) in two case studies and benchmarked against existing analytical and ML-based methods. The applicability of the proposed framework to accommodate diverse transition targets, along with its manufacturability and mechanical performance, is discussed before the conclusion is made.

2. Methodology

2.1. Data curation

The aim is to generate sufficient variations of the target cell types so that clusters with a degree of spread will be formed in the latent space after the training process. The dataset consists of five types of TPMS lattices with diverse 3D geometry and 2D layout at the connecting faces, as shown in Fig. 1. As a surface-based lattice, the unit cell topology is defined by the level set functions, while the volume fraction (VF) is controlled by the offset parameter t (Appendix A). Subsequently, voxel representation is achieved through a spatial discretisation of $100 \times 100 \times 100$ pixels. The choice of resolution is governed by preserving sufficient geometric details whilst making the training process computationally inexpensive. Utilising LatTess [28], an in-house lattice generation software, 200 variants of each TPMS type are equally sampled within the VF range of 0.2–0.6. The lower bound is set to ensure structural integrity while the upper bound prevents diverse cell types from transitioning into a solid block. These data points are further split into training, validation, and testing sets following a ratio of 6:1:1, as a common practice in ML. It should be highlighted that TPMS lattices are chosen for demonstration purposes only, while the methodology is generalisable to any other types of unit cells in voxel representation.

2.2. VAE architecture

A VAE [29] is constructed and trained to map and reconstruct the lattice unit cell to and from the latent space. Fig. 2 illustrates the components of the VAE-based framework. The VAE distinguishes itself from the standard autoencoder by being able to generate clusters in the latent space that are closely packed and potentially overlapping – i.e. enables sensible results to be reconstructed during latent space interpolation, establishing the foundation for latent space arithmetic.

The mean $\mu(x)$ and standard deviation $\sigma(x)$ of each element are obtained through the two ‘parallel’ layers at the end of the encoder as shown in Fig. 2. It implies that the training data are no longer discrete points but continuous regions of normal distribution in the latent space. It increases the degree of overlapping between points within the cluster, allowing continuous clusters to be formed in the latent space and consequently meaningful outputs be re-constructed. The disparity between the reconstructed object from the decoder $\hat{x}$ and the initial input x is termed as the reconstruction loss as expressed in Eq. (1) and is minimised during training. It will, however, not guarantee continuity between clusters.

$$\mathscr{L}_{recon.} = \frac{1}{N}\sum_{i}^{N}(x_i - \hat{x}(z_i))^2 \tag{1}$$

To ensure the clusters are positioned tightly while still being distinct, an additional loss term based on Kullback–Leibler divergence (KL-divergence) is incorporated into the training process. The KL-divergence essentially measures how the probability distributions diverge from each other and its implementation in the VAE can be expressed as:

$$\mathscr{L}_{kl} = \frac{1}{N}\sum_{i}^{N}\frac{(\sigma_i^2 + \mu_i^2 - \log(\sigma_i) - 1)}{2} \tag{2}$$

Hence, the total loss for the training consists of both the reconstruction loss and the KL-divergence as expressed in Eq. (3).

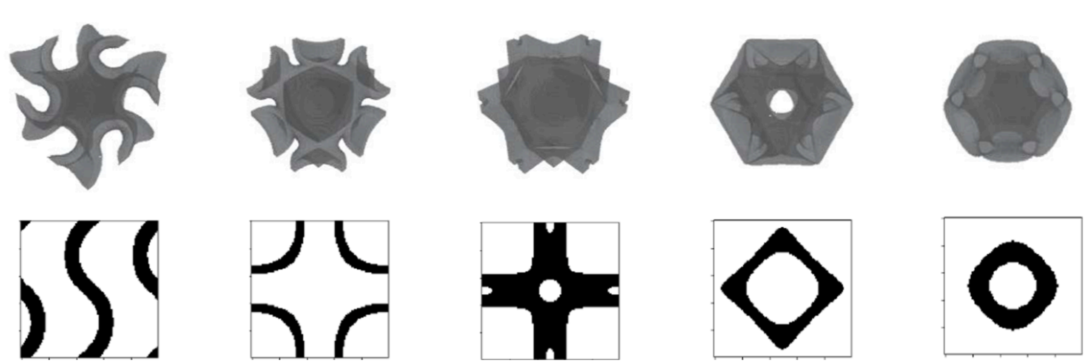

(a) D-Gyroid (b) iWP (c) Neovius (d) Octo (e) Schwartz-P

Fig. 1. Five types of TPMS in voxel representation and the corresponding connecting face.

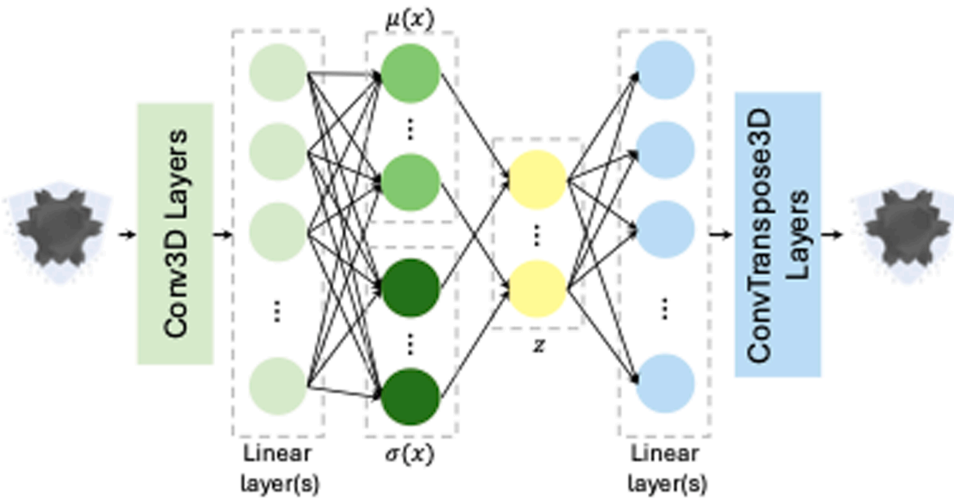

Fig. 2. Architecture of the implemented VAE.

$$\mathscr{L}_{total} = \mathscr{L}_{recon.} + \mathscr{L}_{kl} \tag{3}$$

Three layers of convolution (and transposed convolution) are applied in the encoder (and decoder) to map and reconstruct the unit cells to and from the latent space, as illustrated in Fig. 3. To capture non-linearity, each convolution layer is followed by a Rectified Linear Unit (ReLU) activation function.

The appropriate dimension of the latent space is first suggested by the Principal Component Analysis (PCA) [30] and further confirmed by a parameter study. PCA is conducted on all classes of unit cells through Scikit-learn's PCA function [31] where the cumulative explained variance ratio is obtained up to 50 principal components. The explained variance ratio of a principal component is defined as the ratio between its eigenvalue to the sum of the eigenvalues of all principal components. Hence, the cumulative sum of the explained variation ratios across the principal components reveals the minimum number of components to describe a set percentage of variance in the given set of data. With the orthogonal nature of the principal components, the obtained minimum number can subsequently be used as an indicator of the appropriate latent space dimension in the VAE implementation.

As a result, it is observed that at least 95 % of the variance in the data could be captured once the component number exceeds 12. Subsequently, a parameter study is conducted when the latent space dimension ranges from 8 to 16. There is no significant reduction in the training loss once the latent space dimension exceeds 12, confirming the PCA results. The output from convolution layers is flattened first, followed by a fully connected layer, before feeding into the latent space. Overall, the detailed architecture of the VAE model is presented in Fig. 3. The mini-batch gradient-descent approach is adopted for the training, where the batch size is set as 125 and the optimiser is Adam.

2.3. Transition cell generation

Fig. 4 illustrates the workflow of the transition cell generation. Three main stages of actions are undertaken: i) VAE-based actions; ii) slicing-and-merging; and iii) post-processing. The first stage is conducted within the latent space while the latter two stages take place within the feature space.

2.3.1. VAE-based actions

The target cells are mapped into the latent space through the encoder of the trained VAE. Subsequently, linear interpolation is applied between the two latent vectors at a set interval – either being the same number as the unit cell's resolution N (standard configuration) or multiples of the resolution mN (super-resolution configuration) where m is the user-defined super-resolution factor. The interpolated latent vectors are then fed into the decoder to reconstruct the series of unit cells that are smoothly morphing.

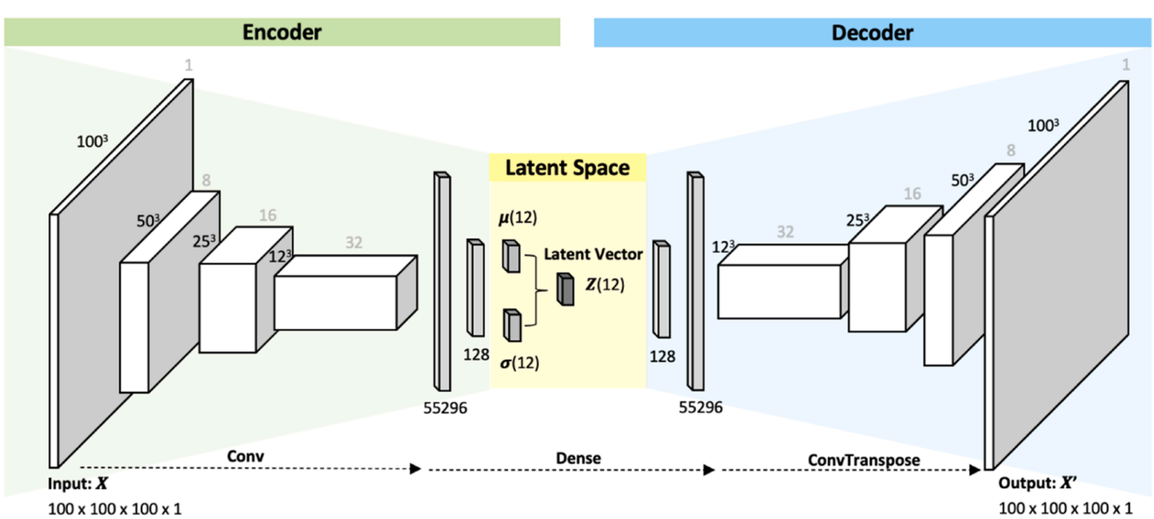

Fig. 3. The detailed architecture of the proposed VAE model.

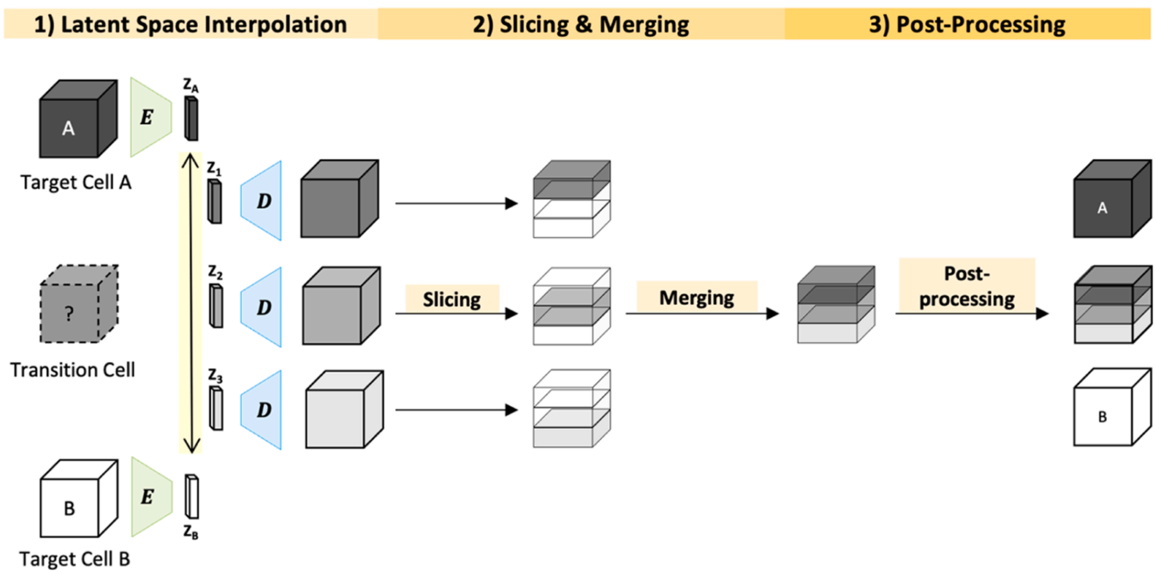

Fig. 4. Workflow for transition cell generation.

2.3.2. Slicing and merging

To ensure full connectivity with the target cells on both ends while preserving the smooth transitioning characteristics of latent-space-based interpolation, an approach of extracting and combining slices from a series of reconstructed unit cells is adopted, hereby termed as 'slicing-and-merging'. The detailed implementation of the strategy for the two possible configurations of a series of unit cells is outlined below:

Standard configuration (the number of unit cells in the series equals to the target resolution value): A series of N unit cells are generated to form the set C. With the subscript denoting the index of the unit cell in set C and the superscript denoting the index of the layer in a cell, the transition cell c is formed as:

$$c^i = C_i^{-i}, \quad i = \{1, \quad 2, \quad \ldots, \quad N\} \tag{4}$$

i.e. the i^{th} layer of the transition cell (c^i) takes the form of the last i^{th} slice of the i^{th} unit cell (C_i^{-i}) in the set.

Super-resolution configuration (the number of unit cells in the series is a multiple of the target resolution value): Set C is formed of mN unit cells. Following the same convention as above, the transition cell c is formed as:

$$c^i = \frac{1}{m}\sum_{j=0}^{m-1} C_{i+j}^{-i}, \quad i = 1 + \{0, \quad 1, \quad \ldots, \quad N-1 \quad \} * m \tag{5}$$

Note that the expression is equivalent to Eq. (4) when the super-resolution factor m is set as 1. The super-resolution configuration with $m = 2$ is employed to generate the outputs presented in the rest of this article unless otherwise stated.

2.3.3. Post-processing

The voxel values in the generated transition unit cell are first converted to binary representation. A threshold value of 0.5 is applied for transition cells generated with the standard configuration, and a threshold value of $\left(1 - \frac{1}{m}\right)$ is applied for those generated with the super-resolution configuration where $m \geq 2$ such that the voxel is assigned a value of 1 only if there is material in most of the constituting slices.

Subsequently, the isolated or loose-hanging elements are removed. Fig. 5 illustrates some cases where secure connection criterion with solely face, edge, or node connection is met, i.e. voxels to preserve. Therefore, for each element, every adjacent face-, edge-, and node-connected element is assigned an adjacency value of 1, $\frac{1}{2}$, and $\frac{1}{4}$, respectively. The face, edge, and node adjacency values sum to an adjacency score for each element. The element is removed if the adjacency score is less than 1 implying no secure connection exists. The operation is run iteratively until the change in total number of elements is less than a user-defined threshold.

Finally, elements are added to fill in the small holes in the resultant transition cell from the previous step with the *remove_small_holes()* function in *scikit-image* library [32]. Fig. 6 illustrates the generated transition cell (with Schwarz-P and Neovius being the target cells, VF =

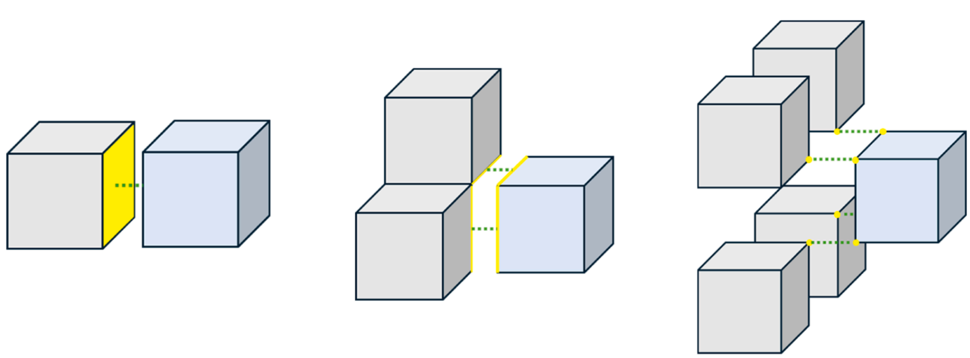

(a) Face (b) Edge (c) Node

Fig. 5. Exploded view to demonstrate the cases reaching secure connection score with only face, edge, or node connection.

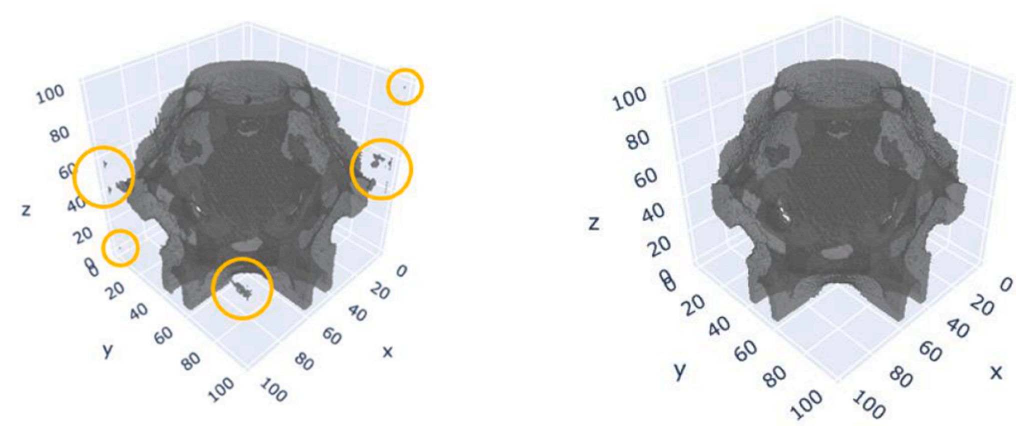

(a) Before post-processing: $VF_{raw} = 0.1837$ (b) After post-processing $VF_{post} = 0.1793$

Fig. 6. Generated transition unit cell before and after post-processing.

0.2) before and after the post-processing.

2.4. Evaluation criteria for a smooth transition

Besides qualitatively assessing the effectiveness of the transition cell generation strategy via visual inspection, quantitative metrics assessing the interfacial connectivity ($C_{\_}$) and geometric similarity ($G_{\_}$) are proposed and defined as:

$$C_A = \frac{|F_A \cap F_T|}{|F_A|} \tag{6}$$

$$G_A = \frac{|X_A \cap X_T|}{|X_A \cup X_T|} \tag{7}$$

where $F_{\_}$ is a 2D array representing the connecting face, $X_{\_}$ is a 3D array representing the unit cell, subscripts A, B, T indicate the two target cells and the transition cell, respectively. The intersection or union between two entities is a voxel-by-voxel comparison.

The connectivity metric needs to be evaluated at both ends of the transition cell for the two dissimilar target cells. Hence, the final performance score is defined as the product:

$$C_{AB} = C_A \bullet C_B \tag{8}$$

$$G_{AB} = G_A \bullet G_B \tag{9}$$

2.5. Case studies

Two case studies are conducted to demonstrate the framework's capability in transitioning between diverse target cell configurations (i.e. different TPMS types and intra-cell VF grading), as shown in Fig. 7. Table 1 summarises the specific target cell configurations.

The proposed framework accommodates graded target cells by tak-

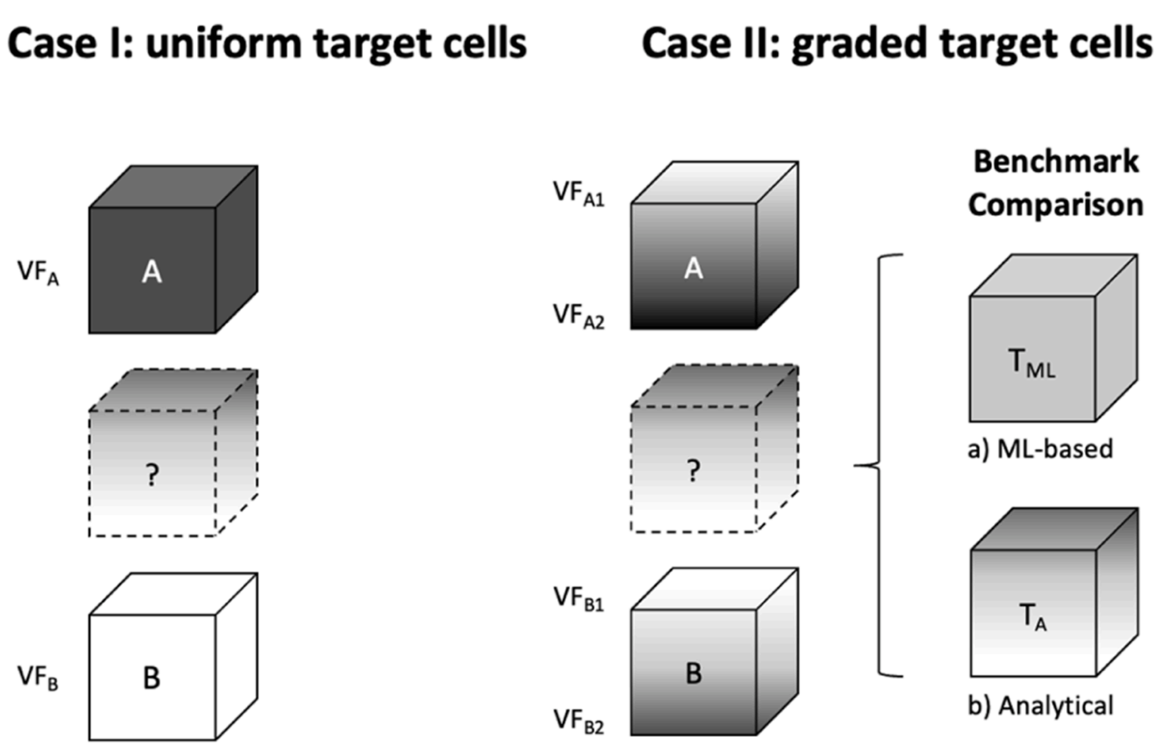

Fig. 7. Overview of the case studies and benchmark methods.

Table 1
Target cell configurations for case studies.

	Unit cell	Lattice type	Volume fraction
Case I	Target A	*Schwartz-P*	0.30
	Target B	*Neovius*	0.50
Case II	Target A	*Schwartz-P*	0.2 – 0.3
	Target B	*iWP*	0.4 – 0.5

ing the VF at the connecting faces (i.e. VF_{A2} and VF_{B1}), which allows the same implementation as the uniform case to be utilised. It is illustrated in Fig. 8.

2.6. Benchmarking

To demonstrate the improvement in interfacial connectivity and geometric similarity, the proposed transition cell generation framework is compared against two benchmark approaches: a) ML-based method and b) analytical morphing. For brevity, illustrations and results in the following sections are based on the graded target cells defined in Case II.

2.6.1. ML-based method

Similar to the proposed methodology, the ML benchmark also builds upon latent space interpolation, but without the "slicing-and-merging" operation applied on the decoded cells. Studies have suggested that the Euclidean distance between two vectors within the latent space implies geometric similarity within the feature space [19]. Fig. 9 presents three equally-spaced interpolation points and the corresponding decoded cells, in which the gradual evolvement in lattice topology aligns with the theory. From a series of interpolated cells, the best candidate is selected to simultaneously maximise two objectives, C_{AB} and G_{AB}, as defined in Section 2.4. Connectivity is prioritised when a global optimum is not present.

2.6.2. Analytical morphing

The analytical benchmark utilises the Sigmoid function to achieve uni-directional morphing between two target cells, as shown by Eqs. (10) and (11). To keep the cell size consistent, the thickness of the morphing region is set the same as the unit cell resolution.

$$\sigma(s) = \frac{1}{1 + e^{-s}} \tag{10}$$

$$X_{analytical} = \sigma \bullet X_B + (1 - \sigma) \bullet X_A \tag{11}$$

where s indicates the spatial information within the morphing region.

3. Results

3.1. VAE training

Fig. 10 indicates that both the training and validation loss converges after 80 epochs, without observing any trend of over- or under-fitting. The training took approximately one hour on an Apple M2 pro chip with 16 GB memory.

Fig. 11 is produced from PCA of the latent vectors in the dataset – the clustering pattern further confirms that the trained model is able to distinguish topological features of different cell types.

Different types of TPMS unit cells are randomly selected from the testing set and serve as the ground truth to compare against the reconstructed ones by the VAE model. High reconstruction accuracy is

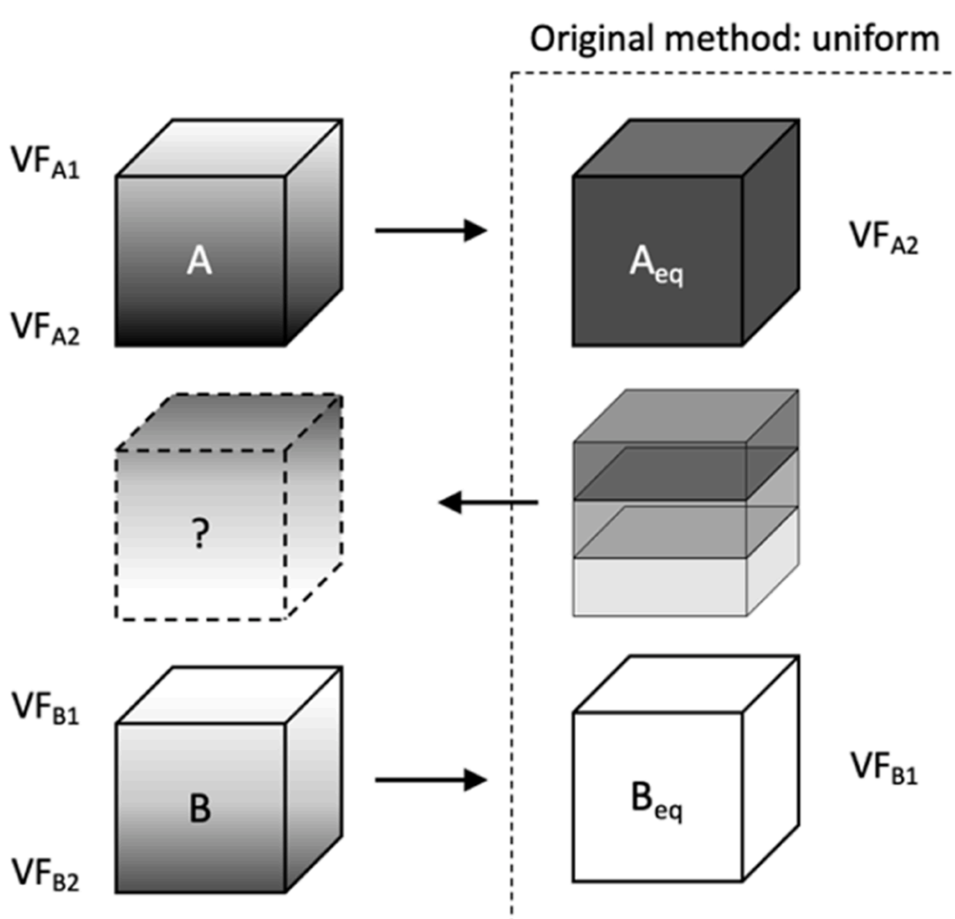

Fig. 8. Modification to the methodology to accommodate graded target cells.

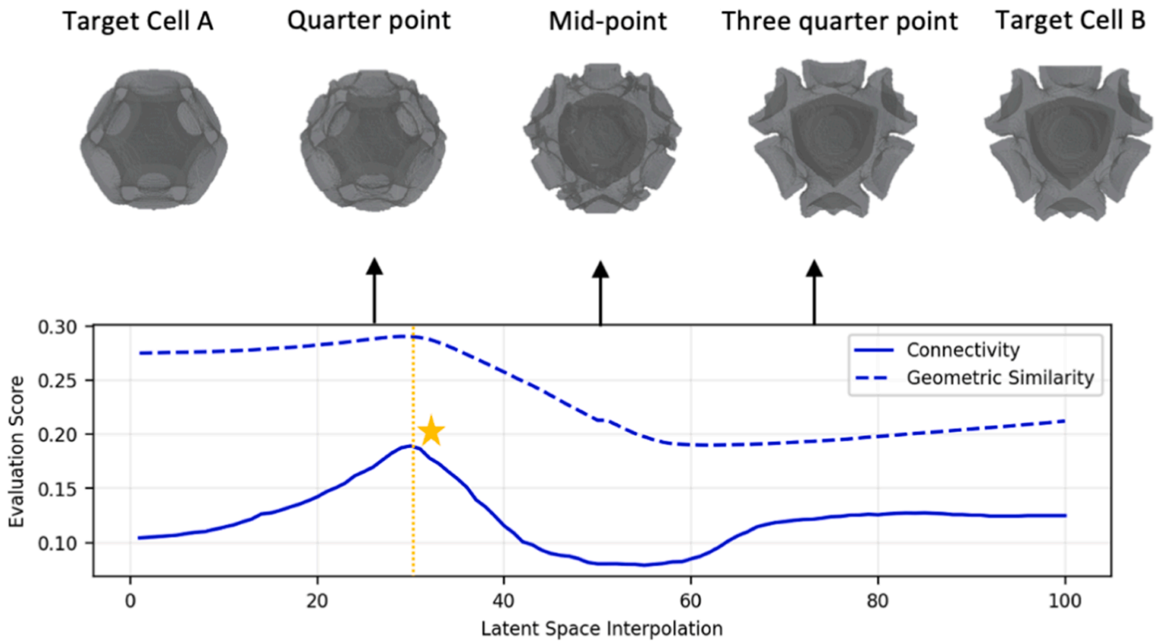

Fig. 9. Unit cells decoded from latent space interpolation.

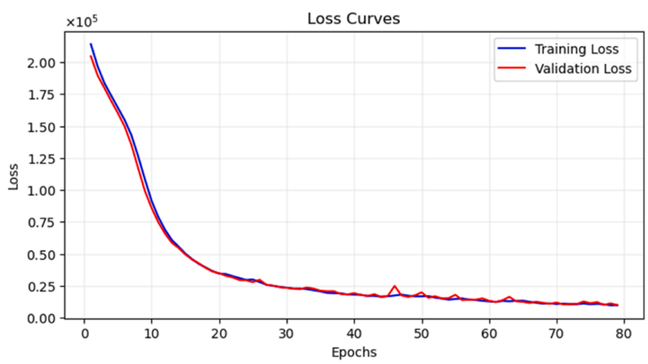

Fig. 10. The training history of the proposed VAE model.

achieved by conducting visual assessment and quantitative evaluation of geometric similarity using Eq. (7), as shown in Fig. 12.

3.2. Smooth transition

Case I. : uniform target cells

Table 2 summarises the specific configuration of the targe unit cells and the quantitative performance of the generated transition cell. Adopting the proposed framework, the generated cell gradually transits from an annulus layout (characteristics of Schwartz-P) to a filleted cross shape (characteristics of Neovius), as shown in Fig. 13. Consequently, the structure is fully connected at both interfaces as desired. The geometric similarity scores are also high, since the transition cell shares some common topological features of the targets, such as central cavity and quadrilateral symmetry. With visual inspection, the transition cell is an intact structure without isolated or loose-hanging elements, proving the effectiveness of the post-processing steps. Although the VF of the transition cell is not a parameter that can be directly controlled, it stays as an intermediate value between the two targets as desired.

Case II. : graded target cells

Table 3 summarises the specific graded target cell configurations and the quantitative performance of the generated transition. Coupled with Fig. 14, a smooth transition with 100 % connectivity at both faces and high geometric similarity is demonstrated.

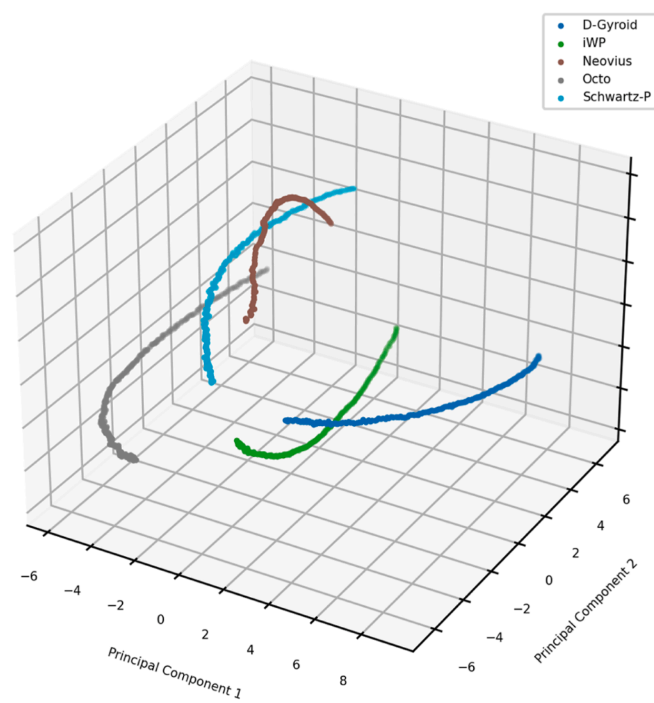

Fig. 11. Shape clustering within the latent space using PCA.

3.3. Benchmark comparison

Qualitative comparisons against benchmark methods are illustrated in Fig. 15 and results from the quantitative evaluations are summarised in Table 4. The proposed method demonstrated full interfacial connectivity compared to both benchmark methods. Since the interpolated cells from the ML benchmark are likely to preserve the symmetric nature of

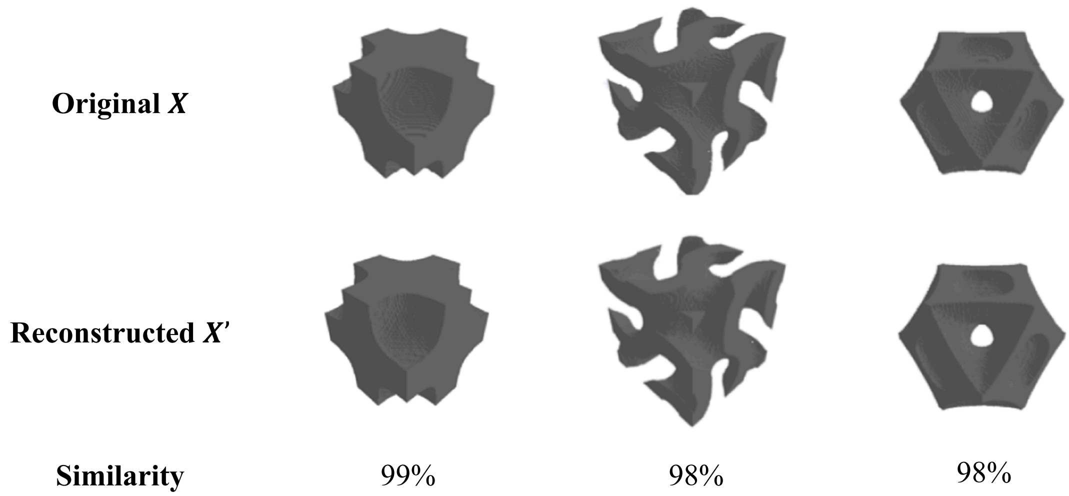

Fig. 12. Compare reconstructed cells with the ground truth in the testing set.

Table 2
Quantitative evaluation for Case I uniform target cells.

Unit cell	Lattice type	Volume fraction $\overline{VF}$	Interfacial connectivity C	Geometric similarity G
Target A	*Schwartz-P*	0.30	1.00	0.72
Target B	*Neovius*	0.50	1.00	0.81
Transition	-	0.41	-	-

TPMS, it is hard to find a universal layout that is well-connected to both faces, especially for dissimilar target cells. Fig. 16 provides a visualisation of the unilateral connectivity issue of cells generated by the ML benchmark method. The interfacial connectivity of the transition generated by the analytical benchmark is marginally lower than that from the proposed framework.

The averaging nature of the analytical benchmark method implies that the geometric similarity to both targets will be comparable in magnitude. Both the proposed method and the ML-benchmark identify the geometrical features in the training and relies on latent space characteristics, such that the generated transition cells are likely to exhibit higher resemblance to one target or the other.

Fig. 15 illustrates that the rendering quality of the analytical benchmark outperforms the proposed method, as the morphing is conducted on implicit functions. Nevertheless, voxel representation makes the proposed method generalisable to non-surface-based unit cells where the analytical benchmark method struggles to generation integral transitions, to be elaborated in Section 4.2.

4. Discussion

While detailed evaluations were provided for two case studies already, the objective of this section is to assess the generality of the proposed methodology. Specifically, visualising the transition between all the other types of TPMS lattice included in the dataset. This enables the exploration of how the geometric differences between target cells affect the smoothness of the generated transition. To prove the proposed framework is not restricted to surface-based unit cells, the transition between truss-based lattices is discussed. Evaluations on manufacturability and mechanical performance have been conducted, though the current framework does not provide explicit control over these aspects.

4.1. Applicability to various TPMS types

Fig. 17 illustrates all the possible combinations resulting from the five TPMS types within the dataset, where the VF of all the target cells were kept at 0.5. Through visual inspection, these transition cells always

Table 3
Quantitative evaluation for Case II graded target cells.

Unit cell	Lattice type	Volume fraction $\overline{VF}$	Interfacial connectivity C	Geometric similarity G
Target A	*Schwartz-P*	0.2 – 0.3	1.00	0.39
Target B	*iWP*	0.4 – 0.5	1.00	0.57
Transition	-	0.35	-	-

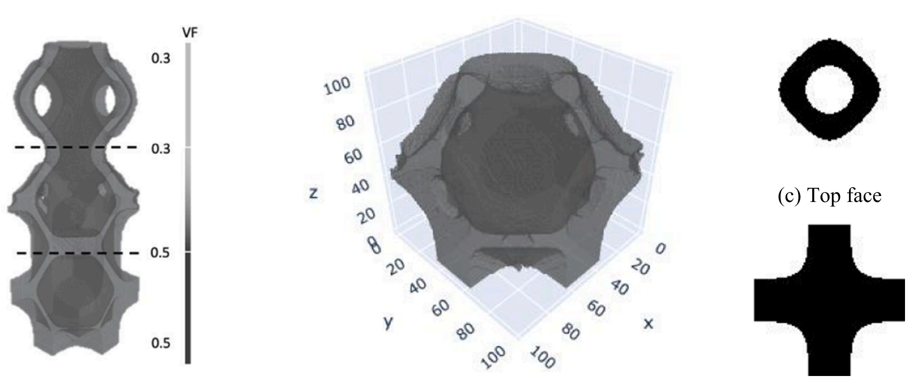

(a) Assembly view (b) Transition cell (d) Bottom face

Fig. 13. Qualitative evaluation for Case I uniform target cells.

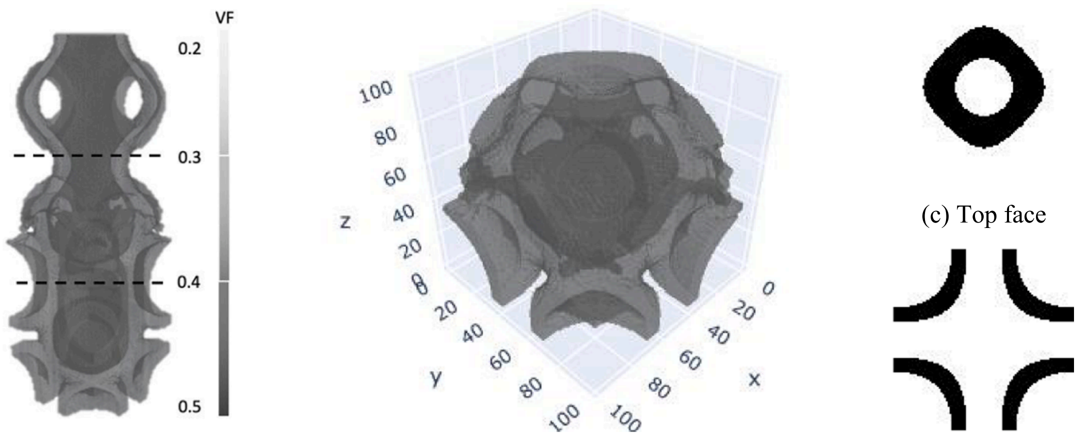

(a) Assembly view (b) Transition cell (d) Bottom face

Fig. 14. Qualitative evaluation for Case II graded target cells.

(a) Proposed method (b) ML benchmark (c) Analytical benchmark

Fig. 15. Qualitative comparison against benchmark methods.

Table 4
Quantitative comparison against benchmark methods.

Evaluation metric		Proposed method	ML benchmark	Analytical benchmark
Volume fraction	$\overline{VF_T}$	0.35	0.32	0.33
Interfacial connectivity	C_A	***1.00***	0.71	0.98
	C_B	***1.00***	0.27	0.95
Geometric similarity	G_A	0.39	***0.74***	0.48
	G_B	***0.57***	0.39	0.48

share geometric features from both targets and high connectivity is guaranteed from the similar interfacial profiles. Detailed quantitative evaluation results for each case are presented in Appendix B. Therefore, it is concluded that the proposed method is adaptable to complex 3D geometries with sufficiently fine resolutions, despite the level of topological dissimilarity between the targets.

To acknowledge the limitation of the algorithm, structural integrity issues might exist for certain target cell configurations when the VF is relatively low (e.g. VF < 0.3). As the example illustrated in Fig. 18, the transition from iWP to Neovius is incomplete when the VF of the target cells is as low as 0.3. The disconnected region gradually encloses from two sides as the VF increases to 0.4. To explain the phenomenon, since the latent vectors interpolated around the mid-point are far away from both targets, the structures become less predictable after decoding back to the feature space. When a significant number of layers were sliced from incomplete structures and then merged, the resulting gap became too large to be redeemed by the post-processing steps. Further research is required to increase the interpretability of the latent space and potentially propose measures to control the latent space characteristics. In the meantime, for practical usage of the proposed framework, it is suggested to determine a lower VF threshold to ensure structural integrity.

4.2. Applicability to truss-based lattice

The voxel representation adopted in the proposed framework implies generality to other lattice types (e.g. truss-based lattice). Following a

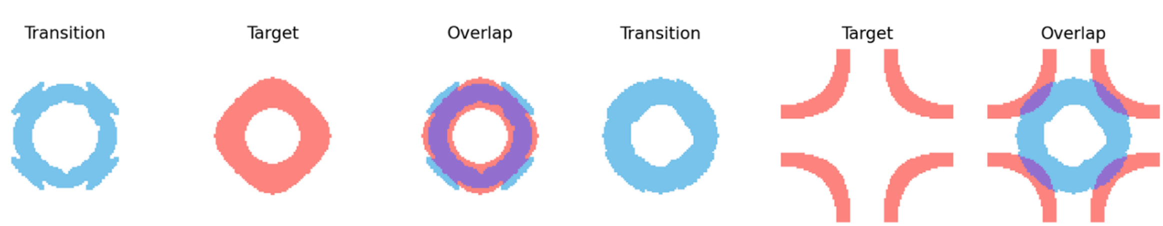

(a) Connectivity with target cell A: $C_A = 0.71$ (b) Connectivity with target cell B: $C_B = 0.27$

Fig. 16. Connectivity visualisation for the ML-based benchmark.

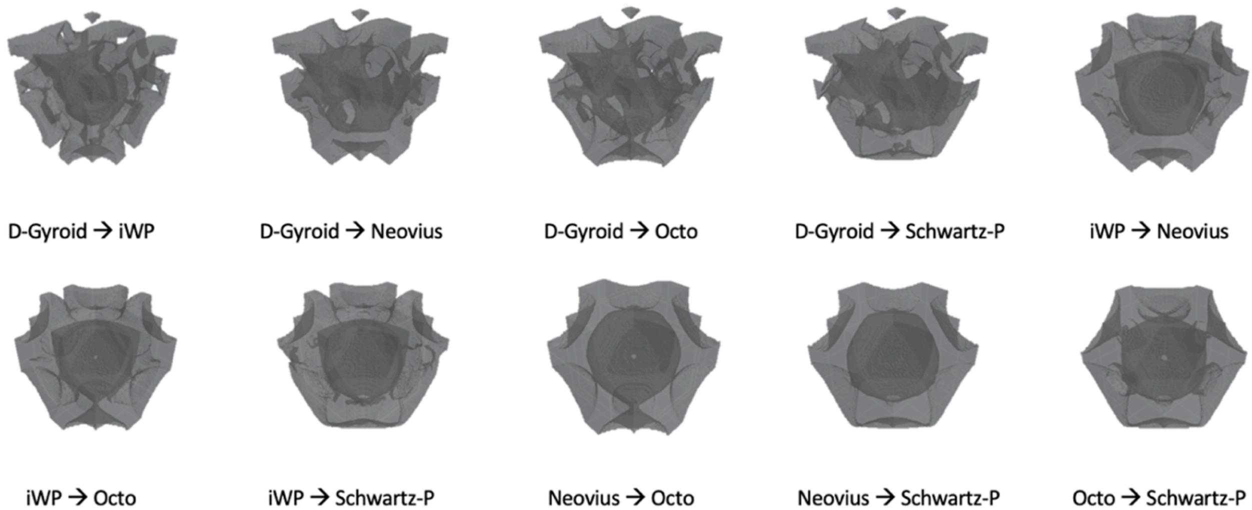

Fig. 17. Transition between various types of TPMS lattice.

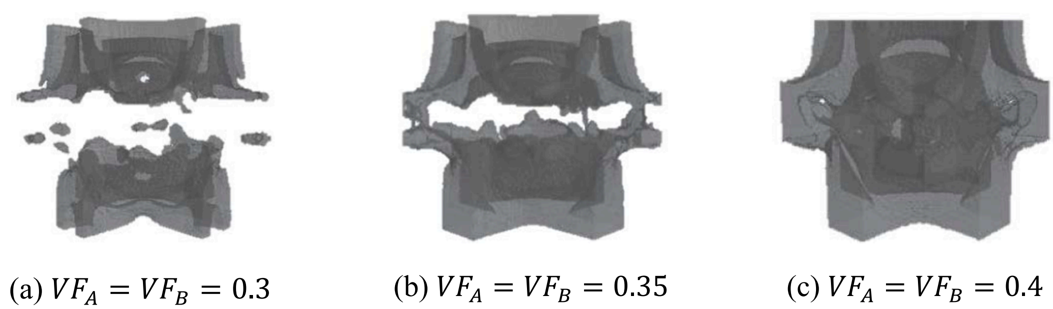

Fig. 18. Structural integrity limitation when the VF of target cells are low.

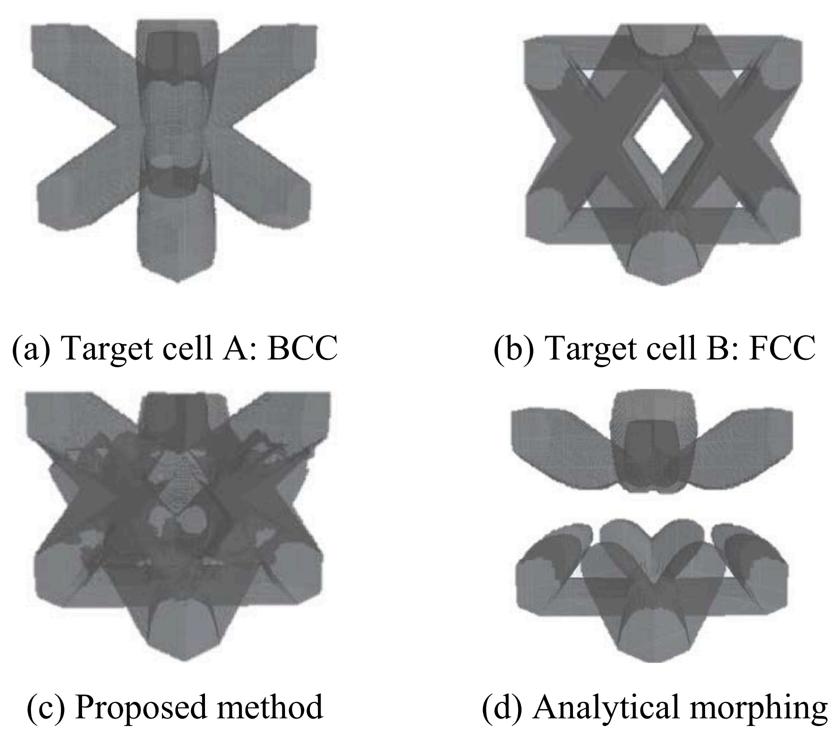

Fig. 19. Transition between truss-based lattice.

similar dataset preparation and VAE training procedure, Fig. 19 demonstrates the transition between a body-centered-cubic (BCC) and a face-centered-cubic (FCC) unit cell, both with uniform $VF = 0.5$. In this case, the proposed method clearly outperforms the analytical benchmark by preserving structural integrity.

4.3. Manufacturability evaluation

With realising multi-unit-cell lattice design being the motivation, the proposed framework establishes the foundation to generate transition cells that are smoothly morphing within a fixed design domain while ensuring full connectivity. It implies that lattices with dissimilar cells can be generated without discontinuity, ensuring the primary manufacturability where the design is integral, as illustrated in Section 4.2.

AM has been a popular choice to fabricate lattice structures for its capability in handling complex geometric features. While the current framework does not incorporate AM constraints explicitly, post-processing steps are in place to remove small or disconnected features which coincide with manufacturing considerations. Overhang angle is one of the most characteristic constraints amongst many general AM design guidelines. By applying the technique outlined in [33], the percentage of elements violating the 45° overhang angle constraint in a transition cell is calculated and presented in Table 5. Most cases achieve a reasonably low percentage of violation. The worse performing cases all has one of the target cells being D-Gyroid which has a relatively large percentage of the elements identified as unprintable. It should be acknowledged that while 45° is a common rule of thumb, some identified unprintable elements may still be printed without support in practice, depending on the fabrication technique and material used.

It can be inferred that the transition cell inherits the target cells' printability. It implies that as long as the target cells are chosen to be printable (e.g. quasi-self-supporting nature of TPMS [34]), the transition cell will be manufacturable even without explicit incorporation of the AM constraints into the framework. Such characteristics enhances the applicability of the proposed framework in generating practical multi-unit-cell lattice designs.

4.4. Mechanical performance evaluation

While the framework does not explicitly incorporate control on the mechanical properties of the generated transition cell, the focus on ensuring smooth and fully connected transition should result in a smooth load transfer throughout the structure. To confirm the hypothesis, uniaxial compression is applied to the assembly of transition cells generated by the proposed and benchmark methods. The finite element simulation is conducted in Abaqus, adopting 8-noded hexahedral element to discretise the design domain. Uniformly distributed pressure load is applied at the top surface while fixed support is applied at the bottom restricting all degrees of freedom. Fig. 20 illustrates the resulting von-mises stress distribution, given Schwartz-P and iWP with uniform VF= 0.5 as the target cells. It is observed that the proposed method achieves high continuity in stress distribution at the interfaces between the transition cell and the targets, comparable to the analytical benchmark's performance. In contrast, significant discontinuities and stress concentration are observed in the ML benchmark, as circled in Fig. 20 (b), corresponding to the location of sudden geometrical change.

The observation highlights that the generated transition cell ensures smooth transition of stress distribution at the same time of ensuring smooth geometrical transition. It implies that lower risk of pre-mature failure at the interface between dissimilar unit cells when the multi-unit-cell lattice is under load. Hence, the local optimisation of the unit cell type can be realised more effectively. Conversely, incorporation of property control on the transition cell is worth exploring to further optimise the local and global performance in addition to achieving geometrical smoothness and full connectivity.

Table 5
Comparison of the percentage of elements violating overhang angle constraint in the transition cells. The top and bottom indicates the printing direction. Percentage of violation in target cells are tabulated in the diagonal entries for reference.

		Target A (top) $VF_A = 0.5$				
		D-Gyroid	iWP	Neovius	Octo	Schwartz-P
Target B (bottom) $VF_B = 0.5$	D-Gyroid	7.6%	10.8%	13.9%	12.7%	9.3%
	iWP	10.7%	7.7%	6.1%	5.3%	4.1%
	Neovius	9.5%	4.2%	6.4%	4.9%	2.7%
	Octo	9.4%	4.2%	4.9%	4.2%	2.2%
	Schwartz-P	6.2%	3.6%	4.0%	4.0%	2.7%

4.5. Application in multi-unit-cell lattice structures

The proposed framework is capable of generating uni-directional transition cell, that is, the two targets are located on the opposite sides of the desired transition region. Nevertheless, its application in multi-unit-cell lattice structures is not restricted in a single direction from the macroscale perspective. Fig. 21 illustrates an example with three regions each dominated by a different TPMS cell type, where the transitions are designed utilising the proposed method. The transition between region A and B (shaded in green) is with uniform VF, however, that between region A and C (shaded in orange) illustrates a more complex case where the VF of target cells increases linearly from 0.3 to 0.5.

The generated transition not only ensures high connectivity at the interface with the targets, but also with the neighbouring transition cells of different VF. For completeness, the intersection of the two transition regions could be designed by applying the union operation on the voxel representation of the two neighbours, though future work is required to strategically optimise for such a scenario.

5. Conclusion

In this paper, a novel transition cell generation framework based on latent space interpolation is proposed. Interfacial connectivity and geometric similarity, as two important evaluation criteria for smooth transition within a multi-unit-cell structure, are simultaneously satisfied within a finite design domain. The effectiveness is demonstrated by the generation of transition between dissimilar cell types as well as those with intra-cell VF grading. The capability of the presented framework will enable realisation of complex metamaterial designs involving multiple dissimilar unit cells in demanding engineering applications. Voxel representation also makes the framework adaptable to target cells without parametric expression, improving its applicability and generality.

Compared to existing ML-based approach, the proposed slicing-and-merging strategy in the feature space significantly improves connectivity – consistently achieving a 100 % score – while preserving the smooth characteristics of latent space interpolation. In addition to achieving comparable performance against the analytical benchmark for TPMS, the proposed framework further demonstrates its versatility in dealing with truss-based lattice.

With the foundation of being able to generate smoothly morphing and fully connected transition cells set in this work, future work aiming to enhance the performance and expanding the features is outlined as following: 1) to address the structural integrity limitation when generating transition between low-VF target cells; 2) incorporation of property control (e.g. mechanical property, thermal conductivity etc.) in the generation of the transition cell. With the current framework limited to uni-directional transition and the generated transition cell inheriting the manufacturability of the target cells, additional capabilities such as multi-directional transition will be developed to further the applicability

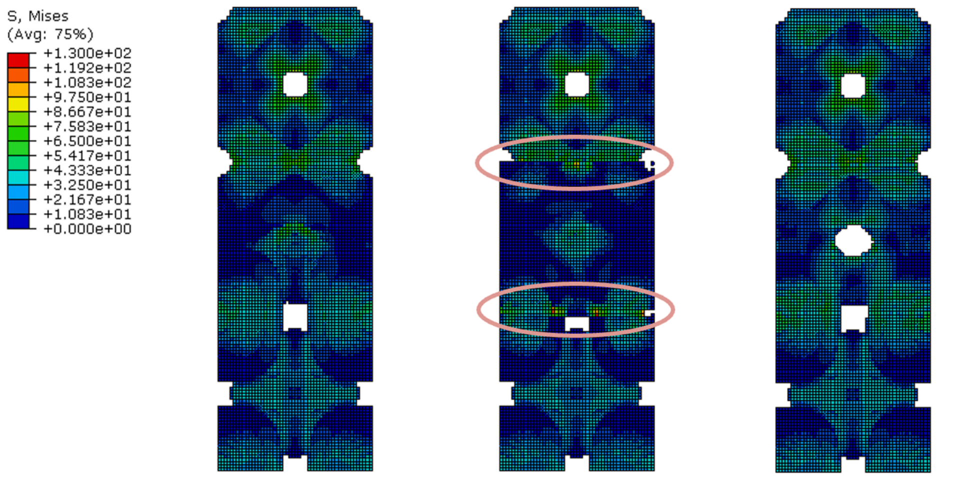

(a) Proposed method (b) ML benchmark (c) Analytical benchmark

Fig. 20. Von-mises stress distribution under uniaxial compression.

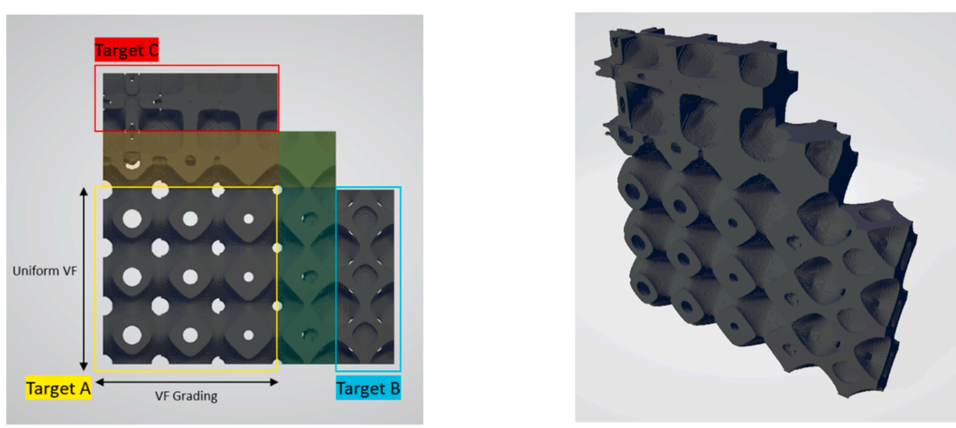

(a) Front view with labels (b) Perspective view

Fig. 21. Apply the transition cell generation strategy in designing a multi-unit-cell lattice structure.

of the proposed framework to more complex real-world applications.

CRediT authorship contribution statement

Xiaochen Yu: Writing – original draft, Visualization, Validation, Software, Methodology, Investigation, Formal analysis, Data curation. **Bohan Peng:** Writing – original draft, Visualization, Validation, Software, Methodology, Investigation, Formal analysis, Data curation, Conceptualization. **Ajit Panesar:** Writing – review & editing, Supervision, Resources, Project administration, Funding acquisition, Conceptualization.

Declaration of Competing Interest

The authors declare that they have no known competing financial interests or personal relationships that could have appeared to influence the work reported in this paper.

Acknowledgements

This work is funded and supported by the Department of Aeronautics at Imperial College London.

Appendix A. The level set functions of TPMS lattices

TPMS Type	Level set function
D-Gyroid	$\lvert \cos(x)\sin(y) + \cos(y)\sin(z) + \cos(z)\sin(x) \rvert \leq t$
iWP	$\lvert \cos(x)\cos(y) + \cos(y)\cos(z) + \cos(z)\cos(x) + 0.25 \rvert \leq t$
Neovius	$\lvert 3[\cos(x) + \cos(y) + \cos(z)] + 4\cos(x)\cos(y)\cos(z) \rvert \leq t$
Octo	$\lvert 4[\cos(x)\cos(y) + \cos(y)\cos(z) + \cos(z)\cos(x)] - 3[\cos(x)\cos(y)\cos(z)] + 2.4 \rvert \leq t$
Schwartz-P	$\lvert \cos(x) + \cos(y) + \cos(z) \rvert \leq t$

Appendix B. Transition between different types of TPMS lattice

Target cells	Transition cell	Volume fraction	Interfacial connectivity		Geometric similarity	
$\overline{VF_A} = \overline{VF_B} = 0.5$		$\overline{VF_T}$	C_A	C_B	G_A	G_B
D-Gyroid → iWP	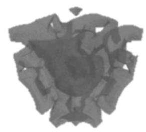	0.49	0.99	1.00	0.41	0.69
D-Gyroid → Neovius	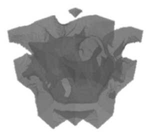	0.46	1.00	1.00	0.40	0.70
D-Gyroid → Octo		0.44	0.99	1.00	0.37	0.63
D-Gyroid → Schwartz-P	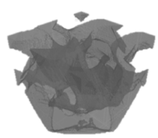	0.46	1.00	1.00	0.39	0.66
iWP → Neovius	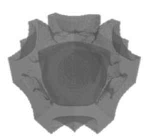	0.56	1.00	1.00	0.67	0.68
iWP → Octo	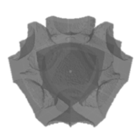	0.55	1.00	1.00	0.78	0.75
iWP → Schwartz-P	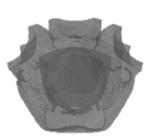	0.56	1.00	1.00	0.73	0.70
Neovius → Octo	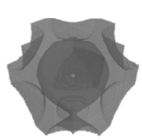	0.54	1.00	1.00	0.87	0.80
Neovius → Schwartz-P	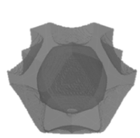	0.52	1.00	1.00	0.86	0.86
Octo → Schwartz-P	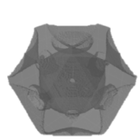	0.53	1.00	1.00	0.84	0.85

Data availability

Datasets generated and codes used during the current study are available from the corresponding author upon reasonable request.

References

[1] T. Maconachie, et al., SLM lattice structures: properties, performance, applications and challenges, Mater. Des. 183 (2019) 108137, https://doi.org/10.1016/j.matdes.2019.108137.

[2] J. Plocher, A. Panesar, Effect of density and unit cell size grading on the stiffness and energy absorption of short fibre-reinforced functionally graded lattice structures, Addit. Manuf. 33 (2020) 101171, https://doi.org/10.1016/j.addma.2020.101171.

[3] A. Takezawa, Y. Koizumi, M. Kobashi, High-stiffness and strength porous maraging steel via topology optimization and selective laser melting, Addit. Manuf. 18 (2017) 194–202, https://doi.org/10.1016/j.addma.2017.10.004.

[4] D.S.J. Al-Saedi, S.H. Masood, M. Faizan-Ur-Rab, A. Alomarah, P. Ponnusamy, Mechanical properties and energy absorption capability of functionally graded F2BCC lattice fabricated by SLM, Mater. Des. 144 (2018) 32–44, https://doi.org/10.1016/j.matdes.2018.01.059.

[5] T.A. Schaedler, et al., Designing metallic microlattices for energy absorber applications, Adv. Eng. Mater. 16 (3) (2014) 276–283, https://doi.org/10.1002/adem.201300206.

[6] Z. Ozdemir, et al., Energy absorption in lattice structures in dynamics: experiments, Int. J. Impact Eng. 89 (2016) 49–61, https://doi.org/10.1016/j.ijimpeng.2015.10.007.

[7] T. Tancogne-Dejean, A.B. Spierings, D. Mohr, Additively-manufactured metallic micro-lattice materials for high specific energy absorption under static and dynamic loading, Acta Mater. 116 (2016) 14–28, https://doi.org/10.1016/j.actamat.2016.05.054.

[8] A. Panesar, M. Abdi, D. Hickman, I. Ashcroft, Strategies for functionally graded lattice structures derived using topology optimisation for Additive Manufacturing, Addit. Manuf. 19 (2018) 81–94, https://doi.org/10.1016/j.addma.2017.11.008.

[9] S. Catchpole-Smith, R.R.J. Sélo, A.W. Davis, I.A. Ashcroft, C.J. Tuck, A. Clare, Thermal conductivity of TPMS lattice structures manufactured via laser powder bed fusion, Addit. Manuf. 30 (2019) 100846, https://doi.org/10.1016/j.addma.2019.100846.

[10] U. Sajjad, T. Rehman, M. Ali, C.W. Park, W.-M. Yan, Manufacturing and potential applications of lattice structures in thermal systems: a comprehensive review of recent advances, Int. J. Heat. Mass Transf. 198 (2022) 123352, https://doi.org/10.1016/j.ijheatmasstransfer.2022.123352.

[11] J. Liu, M. Xu, R. Zhang, X. Zhang, W. Xi, Progress of porous/lattice structures applied in thermal management technology of aerospace applications, Aerospace 9 (12) (2022) 827, https://doi.org/10.3390/aerospace9120827.

[12] W.P. Syam, W. Jianwei, B. Zhao, I. Maskery, W. Elmadih, R. Leach, Design and analysis of strut-based lattice structures for vibration isolation, Precis. Eng. 52 (2018) 494–506, https://doi.org/10.1016/j.precisioneng.2017.09.010.

[13] M. Al Rifaie, H. Abdulhadi, A. Mian, Advances in mechanical metamaterials for vibration isolation: a review, 16878132221082872, Adv. Mech. Eng. 14 (3) (2022), https://doi.org/10.1177/16878132221082872.

[14] L. Cheng, et al., Natural frequency optimization of variable-density additive manufactured lattice structure: theory and experimental validation, J. Manuf. Sci. Eng. 140 (10) (2018) 105002, https://doi.org/10.1115/1.4040622.

[15] D. Li, N. Dai, Y. Tang, G. Dong, Y.F. Zhao, Design and optimization of graded cellular structures with triply periodic level surface-based topological shapes, J. Mech. Des. 141 (7) (Jul. 2019) 071402, https://doi.org/10.1115/1.4042617.

[16] J. Wang, A. Panesar, Machine learning based lattice generation method derived from topology optimisation, Addit. Manuf. 60 (Dec. 2022) 103238, https://doi.org/10.1016/j.addma.2022.103238.

[17] G. Yu, X. Li, L. Dai, L. Xiao, W. Song, Compressive properties of imperfect Ti-6Al-4V lattice structure fabricated by electron beam powder bed fusion under static and dynamic loadings, Addit. Manuf. 49 (2022) 102497, https://doi.org/10.1016/j.addma.2021.102497.

[18] J. Wang, J. Callanan, O. Ogunbodede, R. Rai, Hierarchical combinatorial design and optimization of non-periodic metamaterial structures, Addit. Manuf. 37 (2021) 101710, https://doi.org/10.1016/j.addma.2020.101710.

[19] L. Wang, Y.-C. Chan, F. Ahmed, Z. Liu, P. Zhu, W. Chen, Deep generative modeling for mechanistic-based learning and design of metamaterial systems, Comput. Methods Appl. Mech. Eng. 372 (2020) 113377, https://doi.org/10.1016/j.cma.2020.113377.

[20] L. Wang, Y.-C. Chan, Z. Liu, P. Zhu, W. Chen, Data-driven metamaterial design with Laplace-Beltrami spectrum as "shape-DNA", Struct. Multidiscip. Optim. 61 (6) (2020) 2613–2628, https://doi.org/10.1007/s00158-020-02523-5.

[21] Y.-C. Chen, X. Xu, Z. Tian, and J. Jia, Homomorphic Latent Space Interpolation for Unpaired Image-To-Image Translation, in: Proceedings of the IEEE/CVF Conference on Computer Vision and Pattern Recognition (CVPR), IEEE, Long Beach, CA, USA, Jun. 2019, 2403–2411. doi: 10.1109/CVPR.2019.00251.

[22] L. Mi, T. He, C.F. Park, H. Wang, Y. Wang, and N. Shavit, Revisiting Latent-Space Interpolation via a Quantitative Evaluation Framework, Oct. 12, 2021, arXiv: arXiv:2110.06421. (Accessed 15 March 2024). 2024. (Online). ⟨http://arxiv.org/abs/2110.06421⟩.

[23] Y. Liu *et al.*, Smooth image-to-image translations with latent space interpolations, Mar. 14, 2023, arXiv: arXiv:2210.00841. 2024. (Online) (Accessed 15 March 2024). ⟨http://arxiv.org/abs/2210.00841⟩.

[24] A. Sebestyen, J. Rock, and U.L. Hirschberg, Towards abductive reasoning-based computational design tools, in: Proceedings of the eCAADe (Education and research in Computer Aided Architectural Design in Europe), Novi Sad, Serbia, 2021, 141–150. doi: 10.52842/conf.ecaade.2021.1.141.

[25] J. Wu, C. Zhang, T. Xue, B. Freeman, and J. Tenenbaum, Learning a probabilistic latent space of object shapes via 3D generative-adversarial modeling, in: Proceedings of the thirtieth Conference on Neural Information Processing Systems, 2016.

[26] M. Baldwin, N.A. Meisel, C. McComb, Smoothing the rough edges: evaluating automatically generated multi-lattice transitions, 3D Print. Addit. Manuf. (2023), https://doi.org/10.1089/3dp.2023.0008.

[27] M. Baldwin, Hybrid geometry/property autoencoders for multi-lattice transitions, in: Proceedings of the Thirty Fourth Annual International Solid Freeform Fabrication Symposium – an Additive Manufacturing Conference, Solid Freeform Fabrication 2023, 2023.

[28] A. Panesar, LatTess (Lattice Tessellator). Python, IDEA Lab, Imperial College London, London, United Kingdom.

[29] D.P. Kingma and M. Welling, Auto-Encoding Variational Bayes, Dec. 10, 2022, arXiv: arXiv:1312.6114. doi: 10.48550/arXiv.1312.6114.

[30] I.T. Jolliffe, J. Cadima, Principal component analysis: a review and recent developments, Philos. Trans. R. Soc. Math. Phys. Eng. Sci. 374 (2065) (2016) 20150202, https://doi.org/10.1098/rsta.2015.0202.

[31] F. Pedregosa, et al., Scikit-learn: machine learning in Python, J. Mach. Learn. Res. 12 (85) (2011) 2825–2830.

[32] S. van der Walt, et al., Scikit-image: image processing in Python, PeerJ 2 (2014) e453, https://doi.org/10.7717/peerj.453.

[33] B. Peng and A. Panesar, Application of machine learning in rapid generation of support-free, topologically-optimised structures, in: Proceedings of the AIAA Scitech 2023 Forum, National Harbour, American Institute of Aeronautics and Astronautics, Washington DC, 2023. doi: 10.2514/6.2023-0950.

[34] J. Hu, S. Wang, Y. Wang, F. Li, Z. Luo, A lightweight methodology of 3D printed objects utilizing multi-scale porous structures, Vis. Comput. 35 (6–8) (2019) 949–959, https://doi.org/10.1007/s00371-019-01672-z.